ELSEVIER

Climate change effects on summertime precipitation organization in the Southeast United States

Rosana Nieto Ferreira[a,*], Mark R. Nissenbaum[b], Thomas M. Rickenbach[c]

[a] *Department of Geography, Planning, and Environment, A-227 Brewster Bldg., East Carolina University, Greenville, NC 27858-4353, USA*
[b] *Department of Earth, Ocean and Atmospheric Science, Florida State University, Talahassee, Florida, United States*
[c] *Department of Geography, Planning and Environment, East Carolina University, Greenville, NC, United States*

ABSTRACT

As the earth warms, it is unclear how the organization of precipitation will change, or how these changes will impact regional rainfall and the hydrological cycle. This study combines Weather Research and Forecasting (WRF) model simulations and the pseudo global warming downscaling approach with a precipitation feature identification algorithm to help improve our understanding of the effect of warming on precipitation organization. The WRF model was used to simulate precipitation during a six-day summer period in the southeastern United States under present and future warmer climate conditions. The domain averaged precipitation increased by 45% in the future climate simulation compared to current climate. Modeled precipitation features were classified into either mesoscale precipitation features (MPF) larger than 100 km in length or smaller isolated precipitation features (IPF). In terms of organization, future IPF precipitation fraction decreased while MPF precipitation fraction and feature sizes increased, especially over the ocean, indicating a general increase in mesoscale organization in the future warmer climate. Despite higher thermodynamic instability, future climate IPF precipitation was unchanged over land, possibly responding to stronger subsidence under a strengthened western ridge of the North Atlantic Subtropical High. Yet over the ocean IPF precipitation increased and the amplitude of the IPF diurnal cycle doubled. The most notable precipitation intensity increase, as measured by feature height and rainrate distributions, occurred in oceanic MPFs. These increases in oceanic IPF and MPF precipitation may highlight the role of surface water vapor fluxes in realizing increased precipitation in a warmer climate. This study demonstrates that the application of a simple precipitation feature identification algorithm to WRF simulations can give valuable insight into the effect of climate change upon precipitation organization and intensity. Nevertheless longer simulations are still needed to obtain a robust statistics of the changes of precipitation organization under a warming climate.

1. Introduction

Precipitation organization lies at the heart of the two-way interaction between precipitation and global climate, whereby precipitation drives the atmospheric circulation and is in turn driven by it. Observational and modeling studies have shown that as the earth's climate warms, the mean global precipitation and the frequency and intensity of precipitation extremes will increase (e.g., IPCC, 2014; O'Gorman, 2015; Min et al., 2011). However a gap in our understanding of the effect of climate change on precipitation organization remains, in part because general circulation models can not resolve individual thunderstorms or mesoscale precipitation phenomena (e.g., O'Gorman, 2015; Pendergrass et al., 2016). The focus of this study is to contribute to filling this gap by investigating how precipitation organization in the

southeastern United States (SE US) may change in a warmer climate. This study uses simulations with the Weather Research and Forecasting - Advanced Research Model (WRF-ARW, Skamarock et al., 2008) and the pseudo-global warming approach (PGW, Schär et al., 1996, Frei et al., 1998) to study current and future precipitation organization during a summertime period in the SE US.

Following Rickenbach et al. (2015, hereafter RFZN15) precipitation organization is defined using a simple, size-based framework that is based on whether individual precipitation features attain a mesoscale size threshold of 100 km in maximum horizontal dimension. Previous studies (Leary and Houze Jr., 1979, Rickenbach and Rutledge, 1998, Nesbitt et al., 2000, RFZN15) have identified these mesoscale precipitation features (MPF) to be generally, but not uniquely, associated with synoptic-scale dynamical forcing, while the smaller isolated

precipitation features (IPF) are more commonly associated with local-to-mesoscale circulations and direct thermodynamic forcing. The construct of an MPF, a contiguous region of precipitation of at least 100 km length that is not necessarily of convective origin (Houze, 1989), is useful to study year-round precipitation outside the tropics. A similar precipitation organization classification framework has been used for climatological studies of precipitation systems regionally and globally using surface and space-based radar observations (Rickenbach and Rutledge, 1998, Nesbitt et al., 2000, 2006, Rickenbach et al., 2011, 2013, RFZN15). While MPF and IPF may produce similar time-averaged precipitation totals, especially during the summer season, they can have very different formation mechanisms, climatic feedbacks, and temporal variation (e.g., Schumacher et al., 2004, RFZN15). RFZN15 applied this organization framework to identify IPF and MPF precipitation features in the SE US using a four-year radar-based precipitation dataset. They found that while IPF have a distinct annual cycle, MPF contribute a larger fraction of the total summertime precipitation and occur year round generally in conjunction with the passage of midlatitude cyclones. Nieto Ferreira and Rickenbach (2018) used the RFZN15 precipitation organization dataset to show that the location of the NASH western ridge has a strong influence on the daily variability of precipitation organization in the SE US. They found that the rainiest periods occur when the NASH western ridge is located more to the southwest than usual leading to an increase in MPF precipitation. The driest periods, on the other hand, occur when the NASH western ridge is located northwestward than usual and are associated with suppressed MPF precipitation.

Since mesoscale precipitation organization is not resolved in the coarse future climate model projections currently available, a downscaling approach is needed. This study uses the PGW dynamic downscaling approach (Frei et al., 1998; Schär et al., 1996; Sato et al., 2007 and Kimura and Kitoh, 2007), an approach that preserves present-climate synoptic-scale weather patterns while exhibiting fewer biases than other dynamic downscaling methods (e.g. Yoshikane et al., 2012; Kawase et al., 2008). PGW has been widely used to study the effects of climate change in case-study or climatology mode in problems ranging from regional climate (e.g., Frei et al., 1998; Schär et al., 1996; Sato et al., 2007; Kimura and Kitoh, 2007; Willison et al., 2015), to tropical cyclones (e.g., Hill and Lackmann, 2011 and Kanada et al., 2013), precipitation extremes (e.g., Manda et al., 2014; Lackmann, 2013), tornadic storms (Trapp and Hoogewind, 2016), dust emissions over Asia (Tsunematsu et al., 2011), urban heat islands (Tsunematsu et al., 2011), and snowfall (Hara et al., 2008; Rasmussen et al., 2011). More recently Liu et al. (2017) performed two 13-year WRF simulations over the contiguous US, one under current climate conditions, and a second one under future climate conditions using the PGW approach. Their results showed that the warmer and moister boundary conditions of the future climate simulation lead to an increase in the annual and winter-spring-fall seasonal precipitation. Rasmussen et al. (2017) used the Liu et al. (2017) simulations to analyze changes in convective population and thermodynamic environments in a future climate. They found that convective available potential energy (CAPE) and convective inhibition (CIN) increase in a future warmer climate, contributing to an increase in the frequency of strong convection and a decrease in the frequency of weak to moderate convection, a result that is in good agreement with many previous studies (e.g. Trenberth et al., 2003).

As the climate warms precipitation changes will be driven by changes in atmospheric dynamics via moisture convergence and vertical motion, and changes in thermodynamics via increased temperature and saturation specific humidity (O'Gorman, 2015). Under constant relative humidity, the Clausius Clapeyron equation constrains specific humidity to increase by about 6.5% for each degree increase in temperature (e.g. Allen and Ingram, 2002; Held and Soden, 2006; Pall et al., 2007). Increaseed specific humidity leads to increases in global mean precipitation and extreme precipitation intensity in models (e.g., Hennessy et al., 1997; Kharin et al., 2007; Pall et al., 2007) and

observations (Westra et al., 2013; O'Gorman, 2015). While the Clausius-Clapeyron relationship provides a simple constraint on the increase in precipitation due to thermodynamic changes, the effect of atmospheric dynamics is more difficult to diagnose and quantify. Recently Pendergrass et al. (2016) used idealized aqua-planet simulations to show that as the climate warms atmospheric dynamics can be the main contributor to making convection aggregate into heavily precipitating cloud clusters. Lackmann (2013) also found that atmospheric dynamics was the main contributor to the increases in precipitation that occurred in a pseudo-global warming simulation of a flood event in the SE U.S.

Although there is no clear trend in SE US precipitation in recent decades (IPCC, 2014), the nature of summertime precipitation has become more variable, with larger amplitude changes between wet and dry years favored by a gradual westward shift in the western ridge of the NASH (Li et al., 2013). Future climate simulations in the IPCC CMIP3 dataset suggest that the NASH western ridge will continue to shift westward in the future (Li et al., 2011; Wang et al., 2010), possibly further increasing summertime precipitation variability in the SE US. In addition to changes in the NASH, the SE US is also expected to be affected by a northward shift and weakening of the summertime North American/North Atlantic storm track in a warmer climate, a change that is associated with a poleward shift of the midlatitude jet (e.g., Bengtsson et al., 2006; Barnes and Polvani, 2013) and a decrease in the intensity and number of extratropical cyclones (Bengtsson et al., 2006). However, since the amount of water vapor in the atmosphere is expected to increase (e.g. Allen and Ingram, 2002; Held and Soden, 2006; Pall et al., 2007), the precipitation intensity of individual midlatitude cyclones (Booth and Polvani, 2013) and therefore the precipitation totals along the storm tracks (Bengtsson et al., 2009) are also expected to increase.

In this study two WRF simulations are used to investigate changes in precipitation organization in the SE US in a warmer climate for 16–22 June 2010, a period when synoptic forcing was due mainly to the presence of the western ridge of the NASH. This period was dominated by diurnal forcing with minimal influence of baroclinic systems, thus giving a clearer test of the direct thermodynamic impacts on precipitation organization in a future warmer climate. The diurnal variation of rainfall is also a particularly useful metric to evaluate changes in precipitation variability in the future. In the SE US, summertime convection has a strong afternoon maximum, with a weaker early morning secondary maximum over the ocean (Carbone and Tuttle, 2008; Prat and Nelson, 2014).

This study is organized as follows. Section 2 discusses the study period, datasets, WRF model setup, PGW approach implementation, and precipitation feature identification algorithm used in this study. Section 3 presents a comparison of the precipitation organization in the present climate WRF simulation and in the NMQ observations. Section 4 shows how precipitation feature statistics (sizes and heights, rainfall totals, and rainfall intensity), horizontal distribution and diurnal cycle might change under a future, warmer climate for this particular event. Conclusions are presented in section 5.

2. Datasets and methodology

This study focuses on two summertime WRF simulations, a current climate simulation for 16–22 June 2010 (hereafter WRF-CC) and a future climate simulation for the same period under PGW for RCP8.5 (hereafter WRF-RCP8.5). Details of the modeling approach, datasets, and the precipitation feature organization identification algorithm used in this study are described below.

2.1. Datasets

North American Regional Reanalysis (NARR, Mesinger et al., 2006) sea-level pressure, winds, CAPE and CIN were used to characterize the synoptic-scale conditions during the study period. NARR covers the
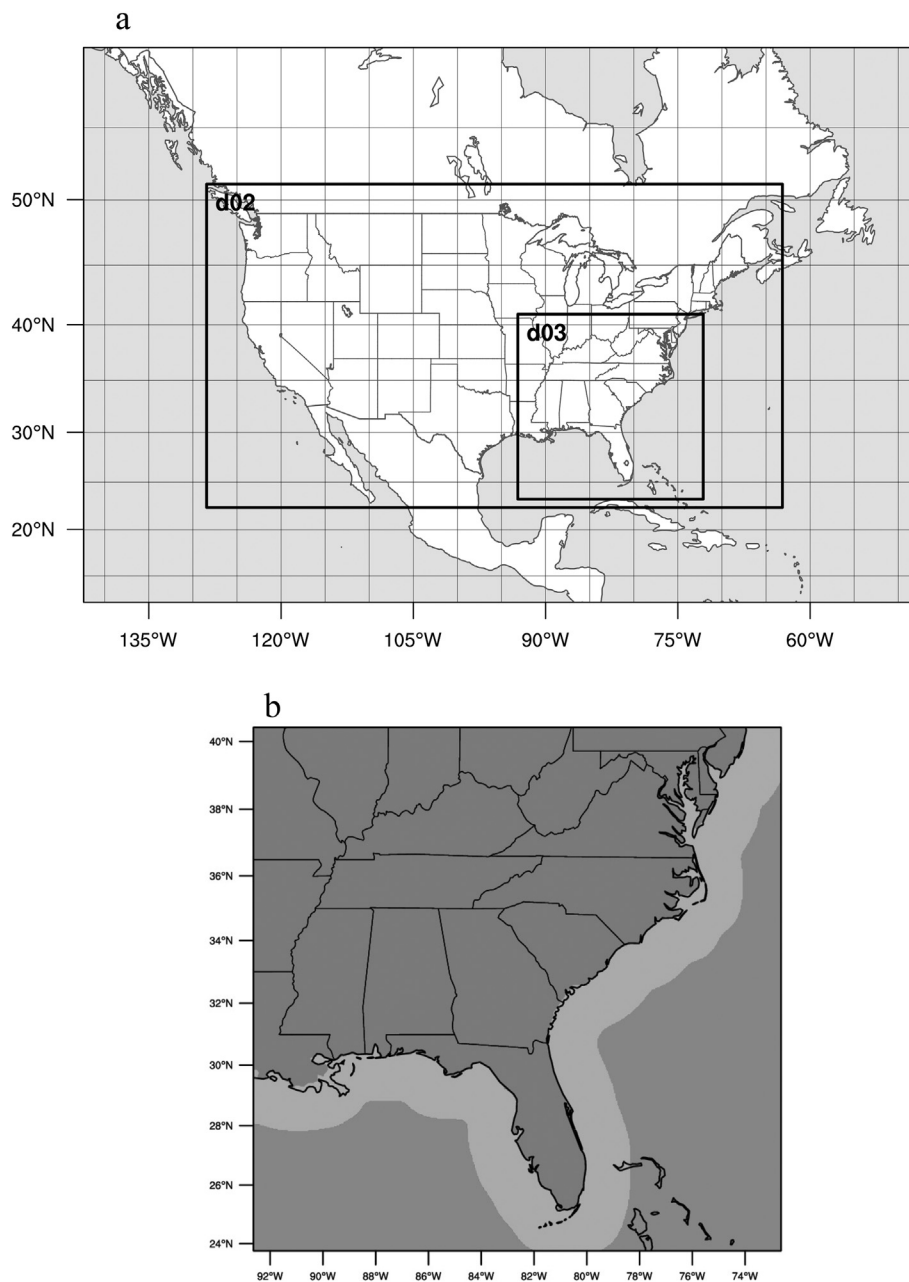
Fig. 1. Domain of model and observations: a) Map of WRF domain configuration showing the 9 km and 3 km inner nests (d02 and d03); b) NMQ radar observation domain over land (gray) and ocean (light gray). There are no radar observations in the dark gray region over the ocean.

North American region and is available 8 times daily at 29 vertical levels and 0.3° (~32 km) resolution. The observed precipitation organization is analyzed using the National Mosaic and Multi-sensor Quantitative Precipitation Estimation (NMQ; Zhang et al., 2011) instantaneous precipitation rates over the SE US and out to approximately 200 km offshore (Fig. 1b). The NMQ precipitation data was constructed from the national network of Next-generation Doppler Radars and terminal Doppler weather radars on a 1 kms grid. The radar-derived precipitation rates were adjusted with rain gage data, and subjected to rigorous quality control (Zhang et al., 2011).

2.2. WRF Model setup

The WRF-ARW version 3.5.1 (Skamarock et al., 2008) was run for a parent domain that covered all of North America and adjacent oceans at 27 km horizontal resolution and two smaller 9 km (d02 in Fig. 1a) and

3 km (d03 in Fig. 1a) resolution nested domains centered over the continental US and the SE US, respectively. Each domain was run with 50 vertical levels. A complete list of physics options (following Lackmann, 2013) is shown in Table 1. Initial and boundary conditions for WRF were provided by the Global Forecast System analysis, a global 1° resolution dataset available four times daily. The 3 and 9 km nested domains received their boundary conditions from the parent domains using one-way nesting. Sea surface temperature data was provided by the National Center for Environment Prediction real-time, global sea surface temperature dataset, a global 0.5° resolution dataset of daily SSTs merged from ship, buoy, and satellite data (Thiébaux et al., 2003). Since sea surface temperature did not change significantly during the simulation, WRF was run with static sea surface temperatures set at the initialization time. At 3 km horizontal resolution WRF begins to explicitly resolve convection and therefore the cumulus parametrization was turned off (Prein et al., 2015) for the innermost domain. WRF

Table 1
Details of WRF grids and corresponding parameterization options.

	Domain 1	Domain 2	Domain 3
Grid Spacing	27 km	9 km	3 km
Microphysics	WRF Single Moment 3 (Hong et al., 2004)	WRF Single Moment 3	WRF Single Moment 6 (Hong and Lim, 2006)
Cumulus Paramaterization	Betts-Miller-Janjic (Janjić, 1994)	Betts-Miller-Janjic	None (Explicit)
Land-surface	Noah (Tewari et al., 2004)	Noah	Noah
Radiation	RRTMG (Iacono et al., 2008)	RRTMG	RRTMG
Boundary Layer	Yonsei (Hong et al., 2006)	Yonsei	Yonsei

simulations were run for a 7 day period from 16 to 22 June 2010, including a 24 h spin-up period (16 June) that is not included in the analysis herein. Output was created every 12 h for the 27 and 9 km domains, and every 15 min for the 3 km domain.

2.3. Future climate simulations and the PGW approach

The future climate simulation was run using a PGW approach implementation similar to that employed by Lackmann (2013) in their study of flooding in the southern United States. In PGW the regional model's initial and boundary condition temperature fields from a present-day analysis product are adjusted using multi-model mean three-dimensional temperature anomalies provided by CMIP5 (Coupled Model Intercomparison Project Phase 5) simulations of future climate change included in the Intergovernmental Panel on Climate Change (IPCC) Fifth Assessment Report (AR5, IPCC, 2014, Taylor et al., 2012). The PGW approach therefore retains present-day synoptic weather patterns in the future climate simulations, allowing a direct comparison of a weather event in the present climate and future climate. The PGW implemented here takes into account only the effects of climate change-related temperature anomalies. It is important to note that more comprehensive PGW implementations that involve adding not only future temperature anomalies, but also other variables have also been carried out. For instance, Liu et al. (2017) chose a more comprehensive PGW approach that included not only temperature anomalies, but also anomalies of future climate horizontal winds, geopotential, specific humidity, soil temperature, sea level pressure, and sea ice. However they found that the strongest anomalies occurred in the thermodynamic fields with weak changes in the circulation fields.

The four warming scenarios in the CMIP5 future climate simulations range from the RCP2.6 low-emissions/low-warming scenario to the high-emissions/high-warming RCP8.5 business-as-usual scenario. The pace of increase in greenhouse gas emissions since the year 2000 is more in keeping with the RCP8.5 scenario (e.g., Sanford et al., 2014), which is predicted to cause global mean temperature increases of up to 4–6 °C by the end of this century (IPCC, 2014). Hence the future climate simulation in this study is forced by temperature anomalies from the RCP8.5 scenario (WRF-RCP8.5). Surface and air temperatures were obtained from historical (from 1850 to 2005) and future climate RCP8.5 emission (from 2005 to 2100) simulations. Five CMIP5 GCMs were selected based on data availability and on the results in Fig. 9.7 of Flato et al. (2013), which evaluated the performance of the climate models represented in CMIP5. The models used to compute multi-model mean (MMM) temperature anomalies are the Australian Community Climate and Earth-System Simulator (ACCESS), the Hadley Global Environment Model 2 and its Atmosphere and Earth System versions (HadGEM2-AO and HadGEM2-ES), the Community Earth System Model

– Biogeochemical Cycle (CESM1-BGC), and the Max Planck Institute Earth System Model running on Low Resolution (MPI-ESM-LR). The MMM temperature anomalies were created by subtracting the RCP8.5 June monthly means for the 2090s from those in the historical run for the 1990s for each GCM and then averaging them all together. This was repeated for surface temperature and three-dimensional air temperature in all three WRF domains. Fig. 2 shows the June MMM surface temperature anomalies for RCP8.5. Over land, surface temperatures increase by 4–7 °C. Given the higher specific heat of water, the temperature increases over the ocean are comparatively more modest at 3–4 °C. Once the temperature anomalies were added to the Global Forecasting System initial conditions the data was read directly into the WRF pre-processing package where geopotential heights and moisture variables were adjusted accordingly. This methodology was implemented with the commonly made assumption that relative humidity in the future warmer remains unchanged from the present climate (Allen and Ingram, 2002, Pall et al., 2007, and Held and Soden, 2006).

2.4. Precipitation feature identification algorithm

The algorithm developed in RFZN15 was used here to classify individual precipitation features according to size as either IPF (smaller than 100 km) or MPF (larger than 100 km) in both the NMQ observations and in the WRF model simulations. The algorithm analyzes each 15-min NMQ and WRF precipitation field, and identifies precipitation features as contiguous gridboxes with rainrates ≥ 0.5 mm/h. Features greater or equal to 100 km in maximum length are placed into the MPF category, with the remaining smaller features placed in the IPF category. The algorithm computes the maximum height and precipitation for each feature, and determines the pixel-based precipitation distribution for IPF and MPF. In WRF, feature heights are calculated by identifying the geopotential height of the highest level with reflectivity greater than or equal to 18 dBZ, the threshold used by the Tropical Rainfall Measuring Mission satellite dataset for climate studies of echo top height (RFZN15). The algorithm was applied to the 15-min WRF precipitation from the 3 km domain, using identical feature size criteria as for the 1 km resolution NMQ data. The coarser grid spacing of the model compared to the observations did not appear to impact the model's ability to simulate IPF and MPF and their structures in instantaneous 3 km WRF-CC images were qualitatively very similar to those in the 1 km NMQ data.

3. Results

To analyze the effect of warming on precipitation organization the current climate WRF simulation (WRF-CC) was first compared to the observations (NMQ) and then to the future climate WRF-RCP8.5 simulation. The emphasis of this analysis is on the IPF and MPF precipitation partition in the WRF simulations.

3.1. Current climate

This section describes the observed synoptic-scale circulation, precipitation patterns, and precipitation organization present during the study period and compares observations to the results from the WRF-CC simulation.

3.1.1. Synoptic-scale overview

During 16–22 June 2010 the synoptic-scale regime was characterized by generally weak forcing for organized precipitation across the SE US. The averaged NARR 250 mb winds (Fig. 3a) show a ridge across the eastern U.S and an upper-level trough over the northwest. The ridge was present on every day of the study period, keeping the midlatitude cyclone track northward across the Ohio Valley and northeastern U.S. At the surface (Fig. 4a) a low-level trough extended southward along the Great Plains from the Dakotas to New Mexico. According to the
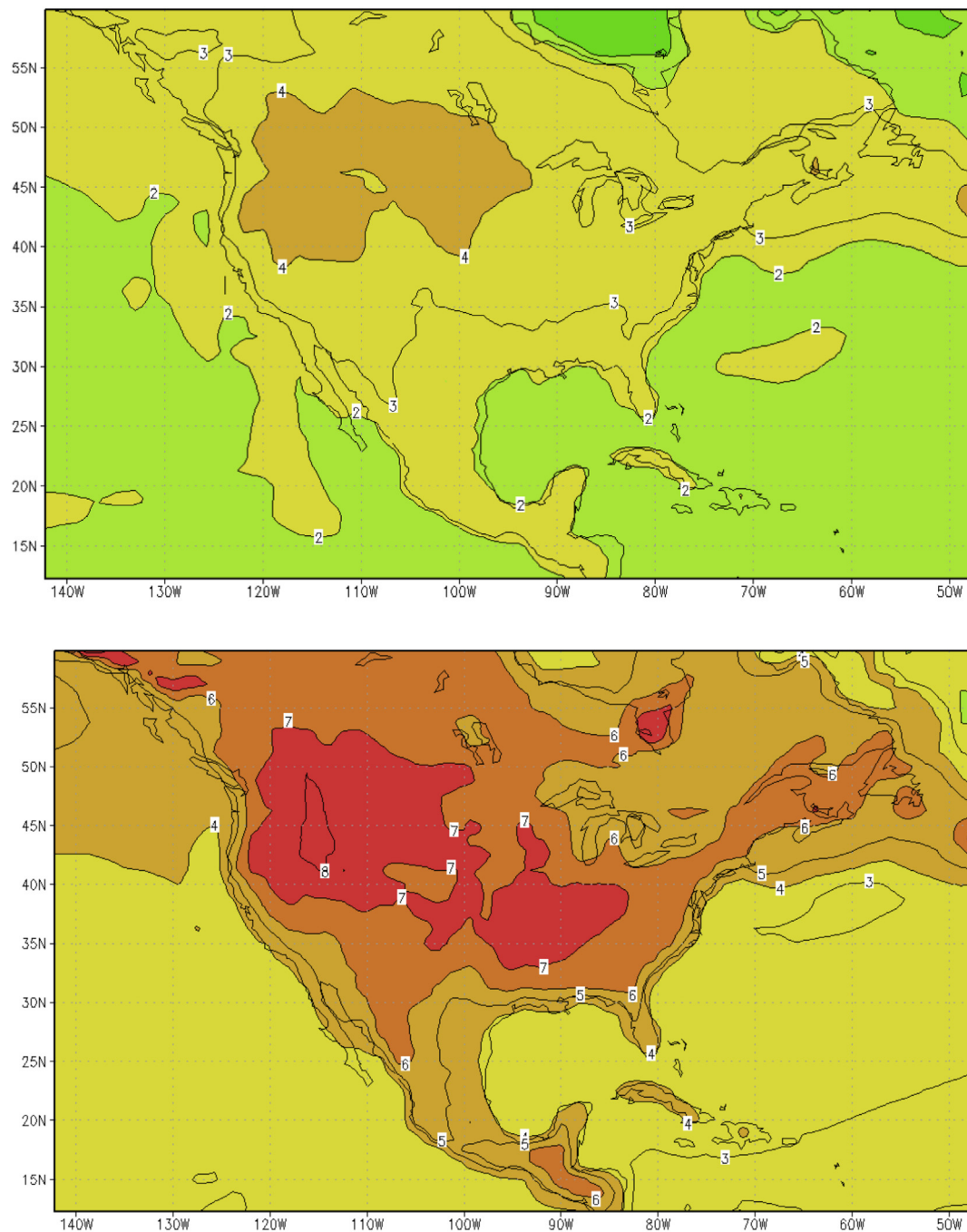
Fig. 2. June MMM surface temperature anomalies for 2090–2100 (in °C) for RCP4.5 (top) and RCP8.5 (bottom).

Nieto Ferreira and Rickenbach (2018) NASH western ridge classification, during June 16–22 2010 the western ridge of the North Atlantic Subtropical High (NASH) was located in the northwest quadrant and extended all the way to the Central Plains. Accordingly, at 850 mb a low-level jet stretched along the western ridge of the NASH from the Gulf of Mexico, northward through TX, OK, KS, and eastward to the Great Lakes (Fig. 3b). Periods like this when the NASH western ridge is located in the northwest quadrant are characterized by weak synoptic forcing for organized convection and tend to be drier than average due to a marked drop in MPF precipitation (Nieto Ferreira and Rickenbach, 2018). The WRF upper and lower level winds (Fig. 3c,d) and sea-level pressure (Fig. 4b) were quite consistent with the NARR. This is to be expected because WRF is updated with analysis fields every six hours.

3.1.2. Precipitation statistics

The precipitation analysis shown here focuses on the domain covered by the 3 km resolution innermost WRF grid (d03 in Fig. 1). The observed accumulated precipitation (Fig. 5a) has several regions of heavy rainfall for the study period. The rain maximum over the Ohio Valley in the northwest corner of the domain (Fig. 5a) is almost entirely associated with MPF (Fig. 5c). This maximum of mesoscale precipitation was associated with two midlatitude cyclones that grazed the northernmost portion of the domain during the study period. Another rain maximum was present in Florida and southern Alabama, Georgia and South Carolina (Fig. 5a). Much of that rain was IPF (Fig. 5b) associated with isolated convection forming each afternoon (RFZN15). Farther south, especially in the Florida peninsula, the MPF rain (Fig. 5c) slightly exceeded IPF (Fig. 5b). Offshore from the Gulf Coast (south of
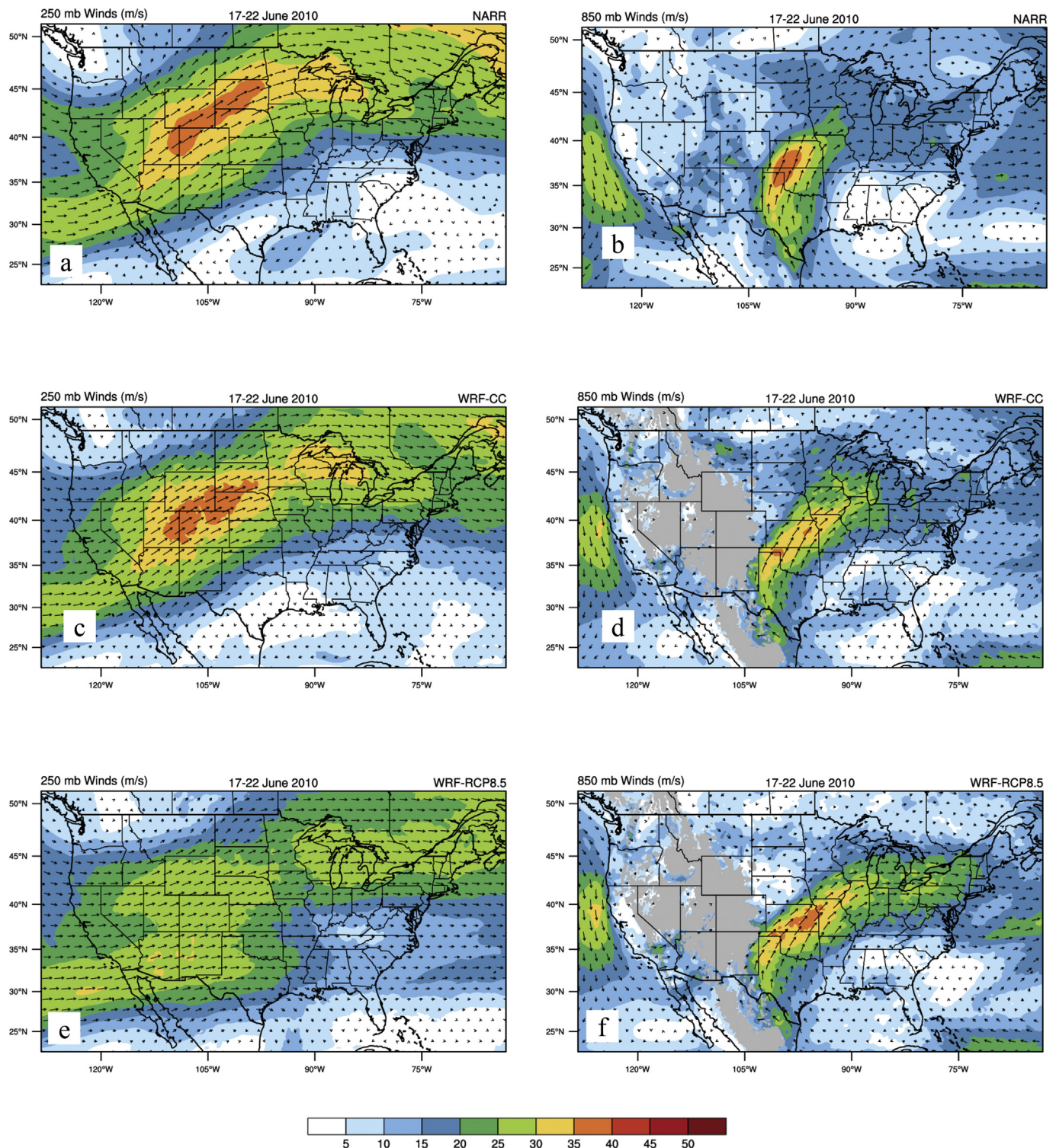
Fig. 3. WRF Upper-level winds (250 mb, left column) and lower level winds (850 mb, right column) averaged from 0000 UTC 17 June to 0000 UTC 23 June in NARR (top row), WRF-CC (middle row) and WRF-RCP8.5 (bottom row).

the Florida Panhandle) a region of heavy rain was present, also with a strong MPF component. Another widespread rain maximum with a strong MPF contribution was located about 100 km off the coast of the Carolinas over the Gulf Stream (e.g., RFZN15). Between the Gulf Stream and the coast, there was a precipitation minimum offshore of the South Carolina, Georgia and northern Florida coasts (RFZN15, RFN18).

Accumulated precipitation maps for the WRF-CC simulation are shown in Fig. 5d-f. In general, although the total WRF-CC precipitation

(Fig. 5d) was weaker, its spatial distribution compares well to the observations (Fig. 5a). While the MPF rain associated with the midlatitude cyclone track in the northern part of the domain was weaker and covered a broader area in the model (Fig. 5f) than in the observations (Fig. 5c), the model reproduced well the observed predominance of MPF rain associated with midlatitude cyclones in the northern domain. To the south, the spatial pattern of the Gulf Coast precipitation and the rain minimum off the South Carolina, Georgia and Florida coast were
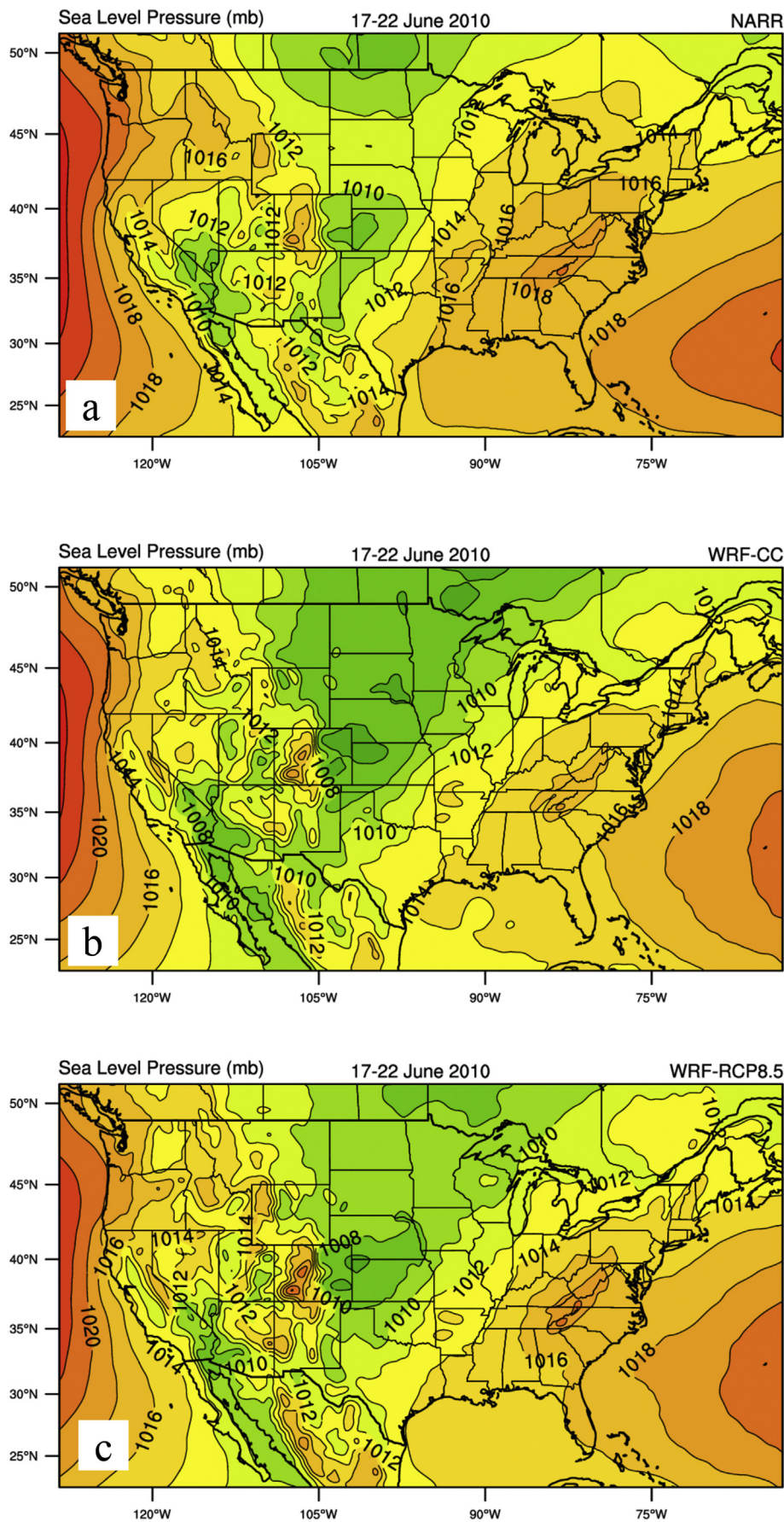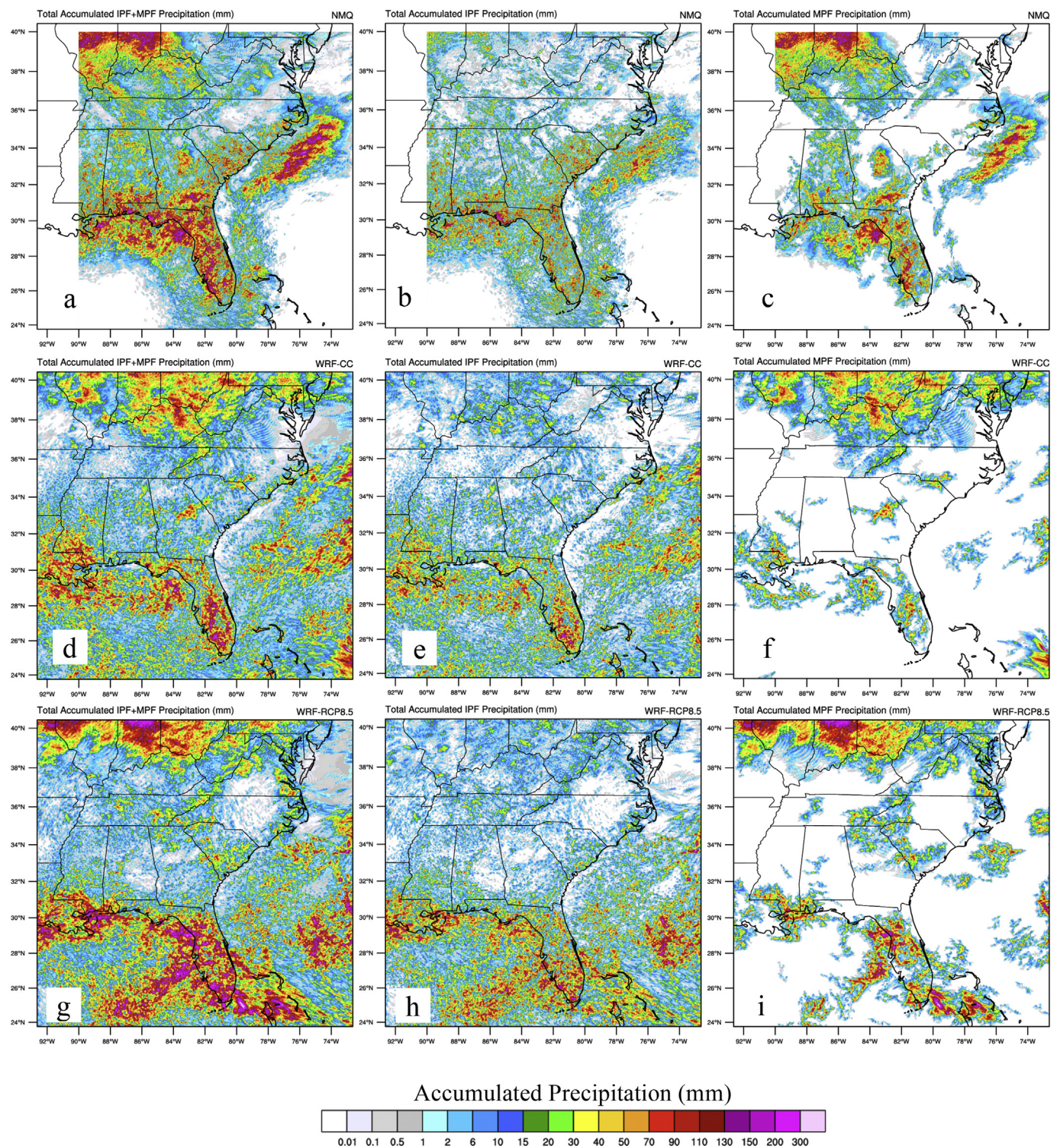
Fig. 4. Sea level pressure (mb) averaged over 0000 UTC 17 June to 0000 UTC 23 June in (a) NARR, (b) WRF-CC, and (c) WRF-RCP8.5.

Fig. 5. Total (left row), IPF (center row) and MPF (right row) precipitation accumulated over 0000 UTC 17 June to 0000 UTC 23 June in NMQ (top row), WRF-CC (middle row), and WRF-RCP8.5 (bottom row).

also well simulated (Fig. 5e). The model tended to slightly overestimate the IPF rain and underestimate the MPF rain in the Gulf Coast region. The model also captured well the IPF precipitation offshore of the Carolinas near the Gulf Stream (Fig. 5e). However, the MPF precipitation along the Gulf Stream was almost completely missed by the model (Fig. 5f) contributing to a deficit in modeled MPF rain over the ocean during the study period.

Table 2 shows accumulated area mean precipitation partitioned by

domain (total/land/ocean) and feature type (IPF/MPF) for the NMQ observations and the WRF-CC simulation. Since the NMQ and WRF domains are different (see Fig. 5a and d), direct comparison of the observations to the model required applying a mask to the model data to make the domains match (Fig. 1b). In this section 'ocean' refers to the masked offshore ocean region common to observations and model, while 'total' domain means 'land' and 'ocean' combined. The rain totals were normalized by domain area (land, ocean, and total) to allow direct

Table 2

Accumulated NMQ and WRF precipitation (mm) normalized by domain area for 17–22 June 2010 and partitioned into IPF and MPF. Percent difference is for simulation relative to observations. Italicized values indicate observed versus simulated differences that are statistically significant to greater than the 90% confidence level; italicized bold values have statistically significant differences to greater than the 99% confidence level.

	TOTAL			
	All	IPF	MPF	Percent IPF
NMQ	20.4	9.8	10.6	48%
WRF-CC	17.6	9.2	8.4	52%
	LAND			
	All	IPF	MPF	Percent IPF
NMQ	24.5	10.6	13.9	43%
WRF-CC	19.2	8.3	10.9	43%
	OCEAN			
	All	IPF	MPF	Percent IPF
NMQ	16.1	9.0	7.1	56%
WRF-CC	13.8	11.4	2.4	83%

comparison of land and ocean rainfall. In the observations, about half (48%) of the total domain precipitation (20.4 mm) was associated with IPF. Precipitation was 20% higher over land than over the ocean. The model underestimated the combined land and ocean precipitation by about 14% (2.4 mm). Overall most of the missing precipitation was MPF. Over the ocean WRF-CC underestimated MPF rain by 4.6 mm (or about 66%) and over land WRF-CC underestimated MPF rain by 3.0 mm (or about 21%) when compared to observations. Though the full domain observed versus modeled IPF precipitation were nearly the same, WRF-CC underestimated IPF rain over land by 2.3 mm and overestimated IPF rain over the ocean by 3 mm. Overall, the model performed better in representing IPF than MPF rain over both land and

ocean. (See Table 2).

Shown in Fig. 6 are frequency distributions of rain rate values over all pixels for all hourly images of the six-day period, with observations shown in black and WRF-CC in gray. Hourly gridpoint rainrate values (including zeros) were distributed into 0.5 mm/h rainrate bins, counted, and normalized by the total number of values so that the sum of all frequencies over all bins is one. The frequency distribution of instantaneous IPF and MPF rain rates for the total domain (Fig. 6, left column) were quite similar for observations versus model. The model captured well the observed logarithmic decrease in relative frequency of pixels with increasing rain rate, and the overall distribution of rain rate values for IPF, MPF and total rain. Note that the lowest limit of frequency is higher for the simulation than the observations, which is an artifact of the difference in resolution between model and observations (the model has fewer grid points over the observation domain). In general, the observed frequency distributions of IPF and MPF were similar for full domain (left column in Fig. 6), land (middle column in Fig. 6), and ocean (right column in Fig. 6). This suggests that the distribution of rain intensity for warm season convection is independent of organization, despite the fact that IPF and MPF features are of different size and likely have different forcing mechanisms. Modeled frequencies were generally similar to observations, with some exceptions. Notable differences include a lower modeled frequency of moderate to heavy rain rates (> 20 mm hr^{-1}) for IPF and MPF over land (Fig. 6, middle column), consistent with the lower modeled rain totals shown in Table 2. Over ocean (Fig. 6, right column), the model overestimated IPF frequency for heavier rain rates (> 40 mm hr^{-1}), while it underestimated MPF frequency for moderate-to-light rain rates (< 40 mm hr^{-1}). It is important also to recognize the possibility of biases in the frequency distribution of precipitation in the NMQ data. For instance, the lower frequency of total observed heavy rain rate over ocean compared to land (Figs. 4 and 5) is possibly a radar range issue.
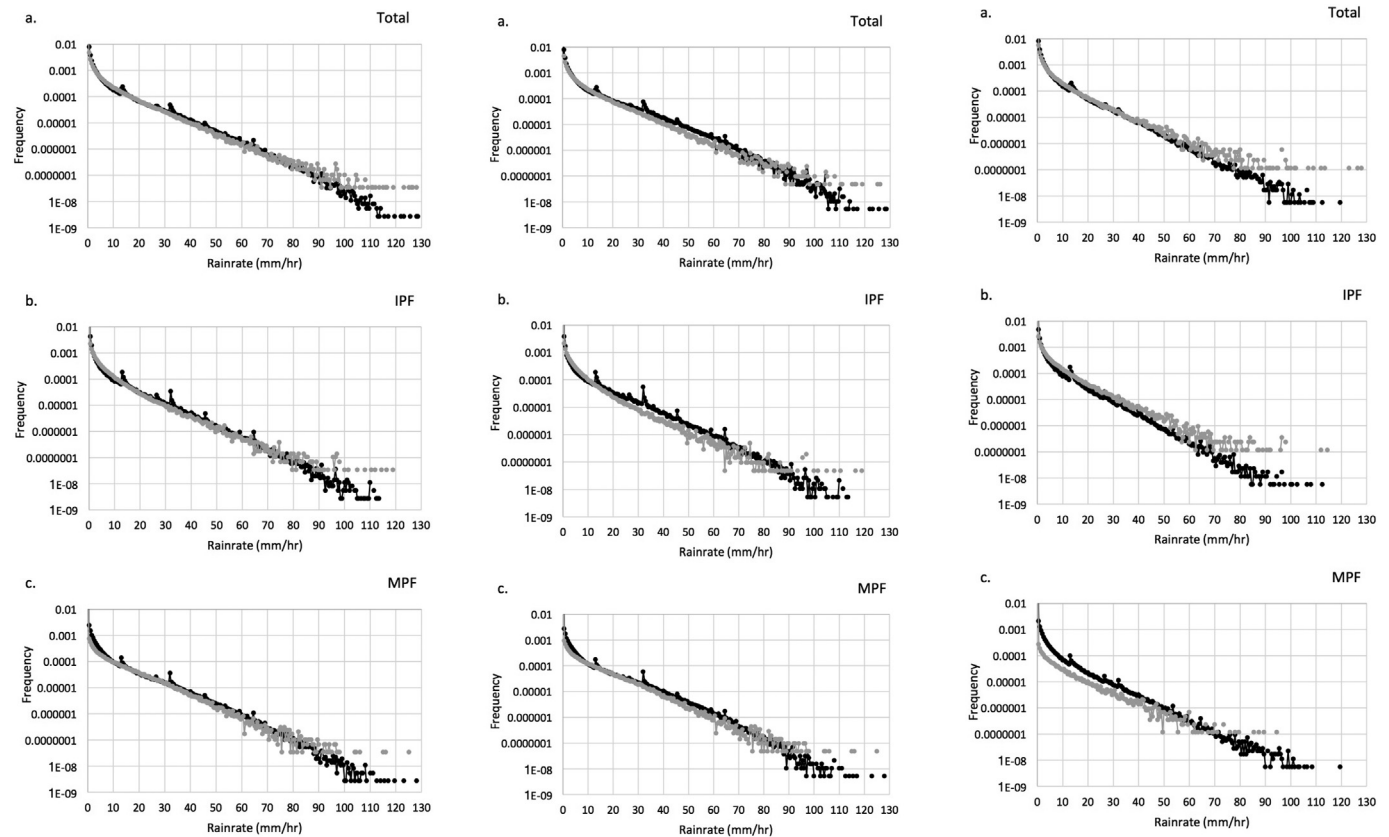
Fig. 6. Frequency distributions of instantaneous values of precipitation (mm hr^{-1}) every 15 min from 17 to 22 June 2010 for all grid points in the NMQ data set (black) and the WRF simulation (gray) for a) total precipitation; b) IPF precipitation; and c) MPF precipitation.
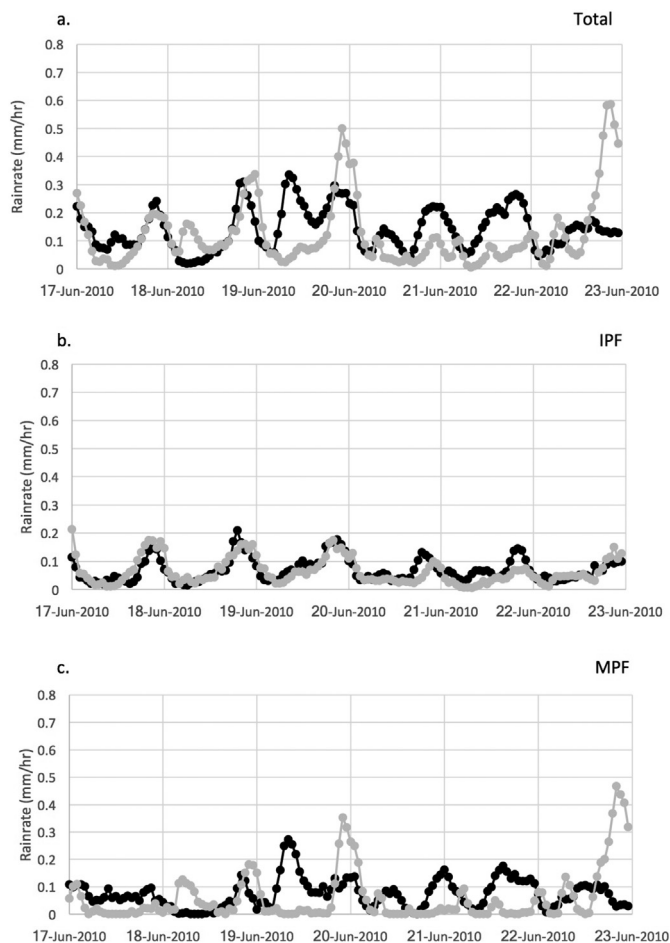
Fig. 7. Time series (UTC) from 17 to 22 June 2010 of hourly observed (black) and simulated (gray) domain-averaged rain rate (mm hr^{-1}) for a) total rain, b) IPF rain, and c) MPF rain over the full radar domain.

Most ocean pixels are at relatively farther ranges to a given radar, resulting in the smoothing of higher rain rates due to larger radar range gate (native pixel) size. The origin of spikes in frequency at discrete rain rate values of 14, 32, and 46 mm hr^{-1} in the observations is not clear, but may be due to small regions of ground clutter missed by the NMQ clutter removal scheme.

The domain averaged hour-to-hour variability of precipitation is shown in Fig. 7. The WRF-CC and observed IPF time series for the full domain (Fig. 7b) were very well correlated (correlation coefficient $R = 0.75$). The WRF-CC and observed MPF time series (Fig. 7c), however, were uncorrelated ($R = 0.05$), as were the total modeled and observed rain time series (Fig. 7a). This suggests that WRF-CC captured well the hourly variation of the observed IPF rain, and that the IPF rain was the component of precipitation that is most predictable - in contrast with the MPF rain. This trend is much clearer in the time variation of precipitation over land (not shown), which shows a clear diurnal variation in IPF rain (consistent with the four-year summer composites shown in Rickenbach et al., 2015). The correlation between observed and modeled IPF rain over land is quite high ($R = 0.83$) with a clear and very regular afternoon maximum (2100 UTC; 1700 LT, where 'LT' refers to Eastern Daylight Savings Time), while there is no correlation for MPF rain (R = 0.05), and a relatively low correlation for total rain ($R = 0.38$). Over ocean (not shown), the observed IPF rain has diurnal variation with a tendency for morning maxima (1200 UTC; 0800 LT) each day, though it is much less clearly defined compared to land. As with land, the modeled total rain and MPF rain over ocean are essentially uncorrelated with observations, but the modeled IPF ocean rain

has a moderate correlation with observations ($R = 0.45$), also with a morning maximum. Both the land and ocean IPF diurnal behavior are quite consistent with previous studies of summer continental rain in the Tropics away from baroclinic forcing (Nesbitt and Zipser, 2003).

In summary, the model captures well the general horizontal patterns of IPF and MPF precipitation but it struggles to capture the amount and areal extent of MPFs, especially over the ocean. The presence of a well-defined forcing for IPF precipitation – the diurnal cycle of heating and cooling - likely contributed to helping the model capture well IPF precipitation amounts, patterns and diurnal variability. In turn, the absence of a well-defined forcing for MPF precipitation, especially under a NASH western ridge northwest regime and away from the midlatitude cyclone influence in the northern portion of the domain, likely contributed to the model's difficulty to capture the observed variability of MPFs, especially over the ocean.

3.2. Future climate

Having established that WRF can capture important characteristics of the precipitation organization variability and distribution, this section turns to comparing the WRF-CC to the WRF-RCP8.5 simulations to study how precipitation organization may change in a future warmer climate. The limited midlatitude cyclone influence makes testing the impact of changes in thermodynamic forcing due to warming using the PGW approach more straightforward.

3.2.1. Synoptic scale overview

Fig. 3c–f shows the upper (250 mb) and lower-level (850 mb) winds for WRF-CC and WRF-RCP8.5 averaged over the study period. Like the observations, both simulations are dominated by the presence of an upper-level trough over the northwestern U.S. and a southwesterly upper-level jet stream that stretches across the central Plains from Arizona to the Great Lakes. When compared to the present climate simulation (Fig. 3c), the future climate upper-level jet stream remained at the same latitude while it became broader, and weakened by about $10 \, \text{ms}^{-1}$ (Fig. 3e). This result is in agreement with the decreased meridional temperature gradient that resulted from the temperature anomalies added to the future climate simulations (Fig. 2). This midlatitude jet behavior is in contrast with previous studies that have shown that as climate changes, the midlatitude jet is expected to shift poleward while keeping about the same intensity (e.g., Bengtsson et al., 2006; Barnes and Polvani, 2013). In the future climate simulation (Fig. 4c) the NASH western ridge strengthened over the eastern US, in agreement with previous studies that showed that the NASH may intensify and encroach further westward as the climate changes (Li et al., 2011). This caused a strengthening of the 850 mb low-level jet by $3–4 \, \text{ms}^{-1}$ in WRF-RCP8.5 (Fig. 3f) when compared to WRF-CC.

3.2.2. Precipitation statistics

The horizontal distribution of total precipitation did not change much under the warmer climate of the WRF-RCP8.5 simulation (Fig. 5g,h,i) when compared to WRF-CC (Fig. 5d,e,f). Both IPF and MPF precipitation increased, particularly along the Gulf coast and Caribbean region (Fig. 8b,c). Compared to WRF-CC, WRF-RCP8.5 also had a dramatic increase in MPF rain associated with the two midlatitude systems in the northern portions of the domain (Fig. 8c), in line with previous studies of precipitation changes around midlatitude cyclones (Bengtsson et al., 2009; Booth and Polvani, 2013). This general increase in model precipitation is consistent with an increase in CAPE as the climate warms. When compared to WRF-CC, domain averaged CAPE increased by 700 J/kg in WRF-RCP8.5, with larger increases over land than over the ocean. Meanwhile domain averaged CIN increased slightly (about 10 J/kg) in WRF-RCP8.5, but remained relatively weak over the domain as a whole.

Table 3 shows accumulated area mean precipitation partitioned by domain (total/land/ocean) and feature type (IPF/MPF). Note that since
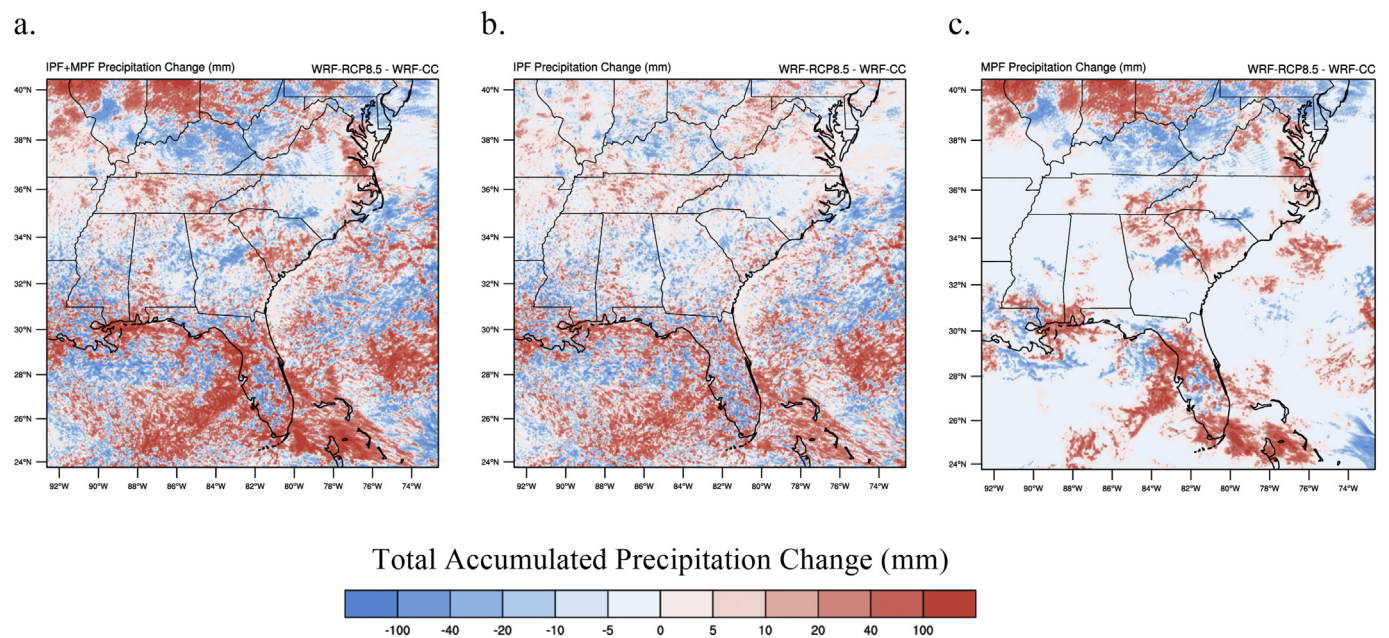
a.

IPF+MPF Precipitation Change (mm)　　　　　　　WRF-RCP8.5 - WRF-CC

b.

IPF Precipitation Change (mm)　　　　　　　WRF-RCP8.5 - WRF-CC

c.

MPF Precipitation Change (mm)　　　　　　　WRF-RCP8.5 - WRF-CC

Total Accumulated Precipitation Change (mm)

-100　-40　-20　-10　-5　0　5　10　20　40　100

Fig. 8. Precipitation differences between future and present climate WRF simulations (WRF-RCP8.5 minus WRF-CC) for a) Total, b) IPF, and c) MPF.

Table 3
Domain averaged precipitation (mm) accumulated from 0000 UTC 17 June to 0000 UTC 23 June 2010, and IPF rain fraction in WRF-CC and WRF-RCP8.5 for the whole domain (ALL), Land, and Ocean. Bold values indicate statistically significant (95%) differences from the corresponding values in the CC simulation.

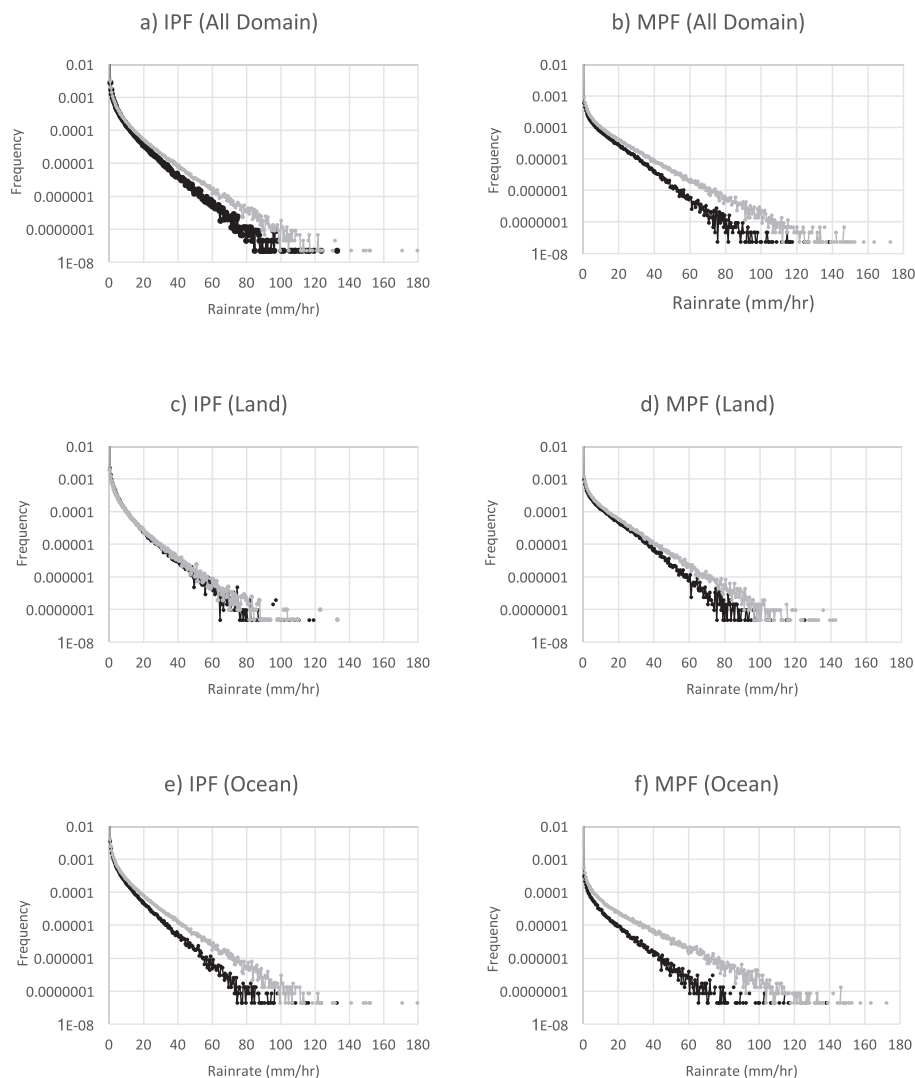|	TOTAL			
	IPF + MPF	IPF	MPF	IPF Fraction
WRF-CC	17.6	11.6	6.0	66%
WRF-RCP8.5	**25.5**	**15.3**	**10.2**	**60%**
	LAND			
	IPF + MPF	IPF	MPF	IPF Fraction
WRF-CC	18.2	8.7	9.5	48%
WRF-RCP8.5	22.5	8.6	**13.8**	38%
	OCEAN			
	IPF + MPF	IPF	MPF	IPF Fraction
WRF-CC	17.0	14.6	2.4	86%
WRF-RCP8.5	**28.5**	**21.9**	**6.6**	**77%**

this section presents a comparison between the two WRF simulations covering the same domain, 'ocean' refers to the whole ocean domain in Fig. 5d-f and not just the portion of the domain within radar range as in section 3.1. The total domain averaged precipitation increased by a dramatic 7.9 mm (45%) in WRF-RCP8.5. The precipitation increase in WRF-RCP8.5 was contributed by ocean IPF (7.3 mm), land MPF (4.3 mm) and ocean MPF (4.2 mm). In contrast, the precipitation total from land IPF remained unchanged, suggesting that IPF precipitation is more sensitive to increased moisture fluxes over a warmer ocean surface than to increased temperatures over land. In the current climate IPF was the favored mode of precipitation with 66% percent of the total rain. Precipitation from IPF was particularly dominant over the ocean, with 86% of the total. In the future climate simulation the IPF precipitation fraction decreased over both land and ocean. These changes indicate that there was a modest but statistically significant shift toward more MPF in the warmer climate. In the warmer climate precipitation increases were larger over the ocean (11.5 mm, or a 67% increase) than over land (4.3 mm km^{-2}, or a 23% increase), despite the fact that RCP8.5 temperature increases were larger over land than over the ocean (Fig. 2), indicating the important role of moisture availability since there is essentially an unlimited water source for evaporation over the ocean.

Fig. 9 shows the hourly rainrate distribution frequency plots for WRF-CC and WRF-RCP8.5. The rainrate frequency distributions were calculated in the same manner as those shown in Fig. 6. In the warmer climate (WRF-RCP8.5, gray lines) rainrates increased as indicated by the distribution shift toward higher rainrates for both IPF and MPF (Fig. 9a,b). Both IPF and MPF experienced the largest rainrate increases over the ocean (Fig. 9e,f) compared to land (Fig. 9c,d). The increased rainfall intensity contributed to the increases in total accumulated precipitation over both land and ocean shown in Table 3. Large rainrate shifts occurred at the high extremes of the rainrate spectrum, and in particular for MPFs. For instance, heavy raining oceanic MPF rainrates increased by up to 40 mm/h from WRF-CC to WRF-RCP8.5 (Fig. 9f). Land MPFs displayed more modest rainrate increases (Fig. 9d). These rainrate increases were in good agreement with previous studies that have shown a shift toward more frequent events of strong precipitation under climate warming scenarios (e.g. Frei et al., 1998; Hennessy et al., 1997; Kharin et al., 2007; Allen and Ingram, 2002, and O'Gorman, 2015; Rasmussen et al., 2017). The results of this study moreover add to the findings of previous studies by demonstrating that the largest increases in instantaneous extreme precipitation in the future warm climate simulations are associated with mesoscale organization over the ocean (Fig. 9f). By contrast, ocean IPF rainrates had a more modest increase compared to ocean MPF. Land IPF experienced almost no rainrate increase in the distribution (Fig. 9c) in agreement with the fact that land-based domain averaged accumulated IPF precipitation did not increase in WRF-RCP8.5 compared to WRF-CC (Table 2).

The diurnal cycle of total precipitation in WRF-RCP8.5 (Fig. 10a, solid black line) shows higher precipitation values than WRF-CC (Fig. 10a, solid gray line) throughout the day but nearly twice the precipitation amount in the morning to early afternoon (0800–1700 UTC; 0400–1300 LT). Upon closer examination the late afternoon (2100 UTC; 1700 LT) diurnal peak over land remains about the same (Fig. 10b, solid lines), while the mid-morning (1400 UTC; 1000 LT) precipitation peak over the ocean nearly doubles (Fig. 10b, double lines). This increased mid-morning peak over the ocean is nearly entirely due to an increase in IPF precipitation (Fig. 10, double lines). The phase of the diurnal cycle over land and ocean remains the same as that in WRF-CC.

In addition to rainrates and total feature precipitation the precipitation feature identification algorithm also produces information on

Fig. 9. Total, land and ocean frequency distribution of IPF and MPF rainrate for 0000 UTC 17 June to 0000 UTC 23 June 2010. WRF-CC (black) and WRF-RCP8.5 (gray).

feature sizes and maximum heights. Fig. 11 shows the feature length distributions for WRF-CC and WRF-RCP8.5 over the entire domain, and partitioned between land and ocean. The warmer climate displayed a shift toward larger features over the ocean, as indicated by the fact that larger IPFs (between 50 and 100 km lengths) and MPFs became more numerous in the warmer climate. Feature lengths were basically unchanged over land (Fig. 11b).

The maximum feature height distributions for WRF-CC and WRF-RCP8.5 are shown in Fig. 12. Maximum feature heights are related to the vertical intensity of the convection. Comparison of feature heights for the present and future WRF simulations revealed important trends. The WRF-RCP8.5 maximum feature height distributions for IPF and MPF were generally similar in shape to those of the current climate but a few important changes. The IPF feature height distribution is bimodal with mostly shallow (2–8 km) IPF and a weak secondary peak at 12–14 km (Fig. 12a). The MPF population had a single maximum fearture height peak between of 10–18 km (Fig. 12b). Simulated shallow IPF were three times more numerous over ocean than land, even though the land and ocean area of the inner model domain were similar. Deep IPF had a similar number of features over land and ocean. In the WRF-RCP8.5 simulation both IPF and MPF underwent a shift toward deeper features (Fig. 12a,b). For the IPF this shift is indicated by a decrease in the number of shallow features (4–6 km in height) and an

increase in the number of deep features (12–16 km). The MPF feature height distribution maximum shifted from 14 km in the current climate simulation to 16 km in the WRF-RCP8.5 simulation. These changes in MPF height distribution were similar for land and ocean. In general, the increase in feature heights as the climate warms was consistent with the increases in CAPE and increase in depth of the troposphere in WRF-RCP8.5. The presence of deeper features can also help explain the higher rainrates that occurred in WRF-RCP8.5. Similarly Lackmann (2013) suggested that the increased rainrates in his future climate PGW simulation of a flooding event in the SE US were due not only to an increase in specific humidity, but also to the presence of an elevated troposphere, higher CAPE and more intense upward vertical velocities.

In summary, the results presented here suggest that in a warmer climate consistent with the RCP8.5 scenario the size and depth of precipitation features could increase and contribute to an increase in rainrates and total precipitation amounts. This shift toward larger and deeper precipitation features could contribute to a shift to higher MPF precipitation fractions under a warmer climate.

4. Conclusions

This study is a step toward filling the gap in our current understanding of the effect of climate change on precipitation organization.
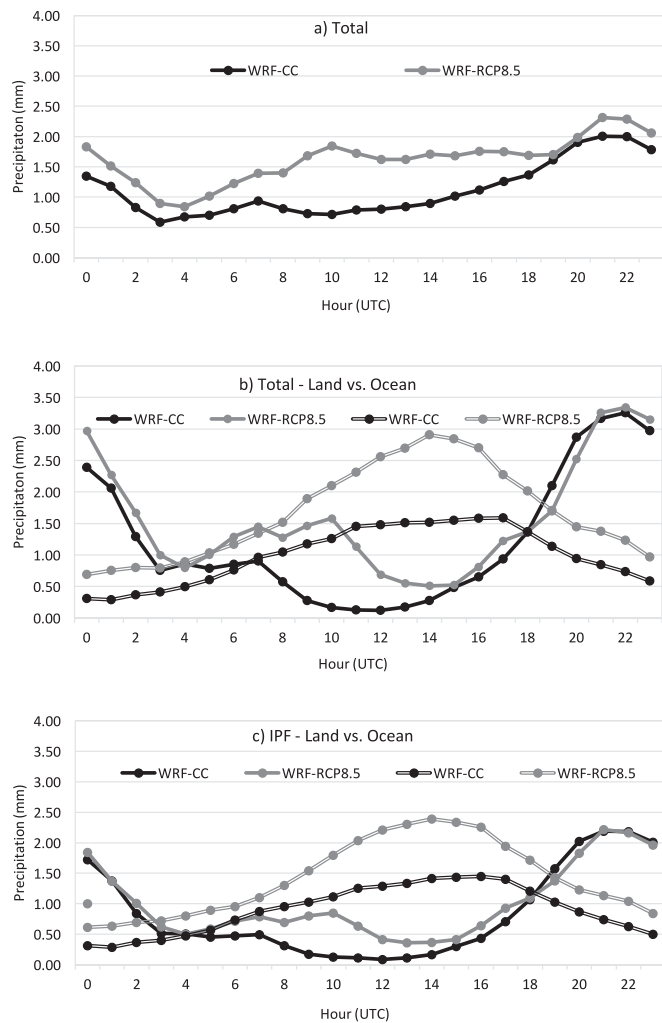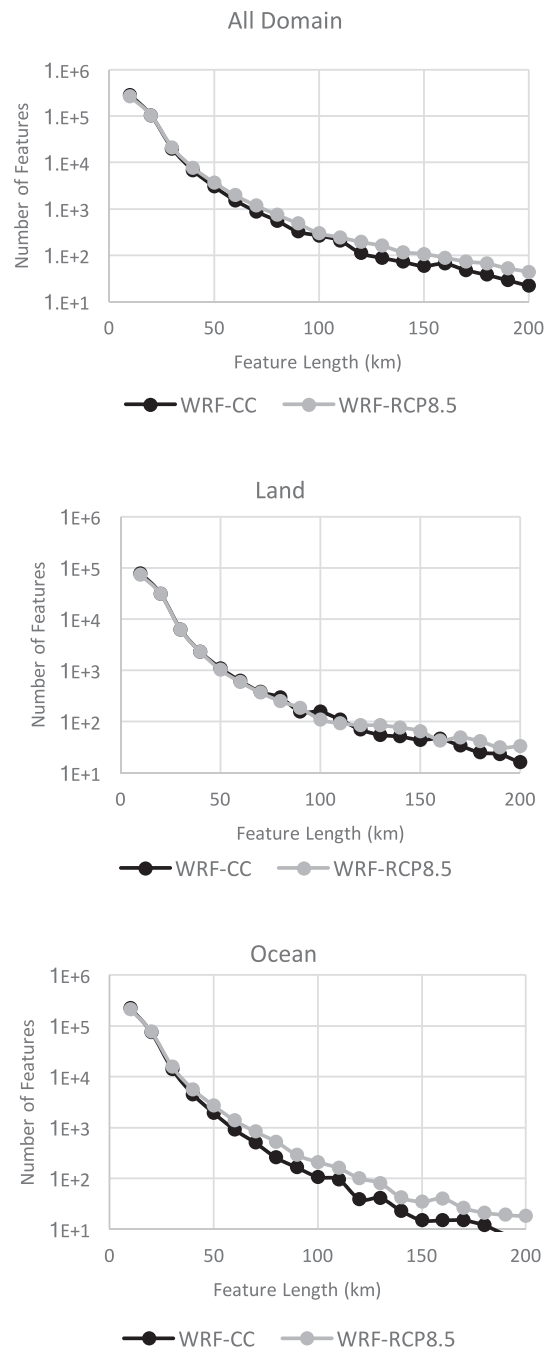
Fig. 10. Mean diurnal cycle of precipitation during 0000 UTC 17 June to 0000 UTC 23 June 2010. WRF-CC (black) and WRF-RCP8.5 (gray) for land (single line) and ocean (double line).

The RFZN15 precipitation feature organization classification algorithm was applied to six-day long current and future climate WRF simulations during the summer of 2010. Though the short simulations in this study do not yield general conclusions about the effect of climate change on precipitation organization, they do provide initial insight and suggest a path forward to addressing this problem.

This study provides a first look at the effect of climate change on precipitation organization in the SE US during a relatively undisturbed period dominated by the presence of a northwest-displaced NASH western ridge and limited baroclinic influence. In this NASH-dominated case, the diurnal variation of rain was tied mainly to IPF formation, with an afternoon rain maximum over land and a weaker morning maximum offshore. A comparison between the model and observed precipitation organization for the study period showed that though the model reproduced well the spatial distribution of IPF and MPF precipitation, it underestimated MPF precipitation, particularly over the ocean. The model also captured well the observed frequency distribution of rain rate values for IPF, MPF and total rain, though it somewhat overestimated the frequency of heavy oceanic IPF rain and underestimated the frequency of light MPF rain. The observed frequency distributions of IPF and MPF instantaneous precipitation were similar for land, ocean and full domain suggesting that the distribution of rain intensity for warm season convection is independent of organization, despite the differences in size and forcing mechanisms for IPF and MPF.

Fig. 11. Feature length distribution during 0000 UTC 17 June to 0000 UTC 23 June 2010 for WRF-CC (black) and WRF-RCP8.5 (gray) for land and ocean.

The model captured well the hourly variation and diurnal cycle of IPF precipitation, but not MPF precipitation. This suggests that the IPF precipitation was more predictable than MPF precipitation during the study period, likely due to the presence of a well-defined thermodynamic forcing mechanism for IPF precipitation during this NASH-dominated period.

Compared to the current climate simulation, the future climate simulation produced a weaker and broader jet stream over North America (in good agreement with the results of Liu et al., 2017). In the lower troposphere the NASH became stronger leading to a stronger low-level jet over the Great Plains and a stronger moisture flux toward the Great Lakes and northern portion of the 3 km WRF domain. In the warmer climate the horizontal distribution of precipitation remained similar to that of the current climate. Precipitation totals however,
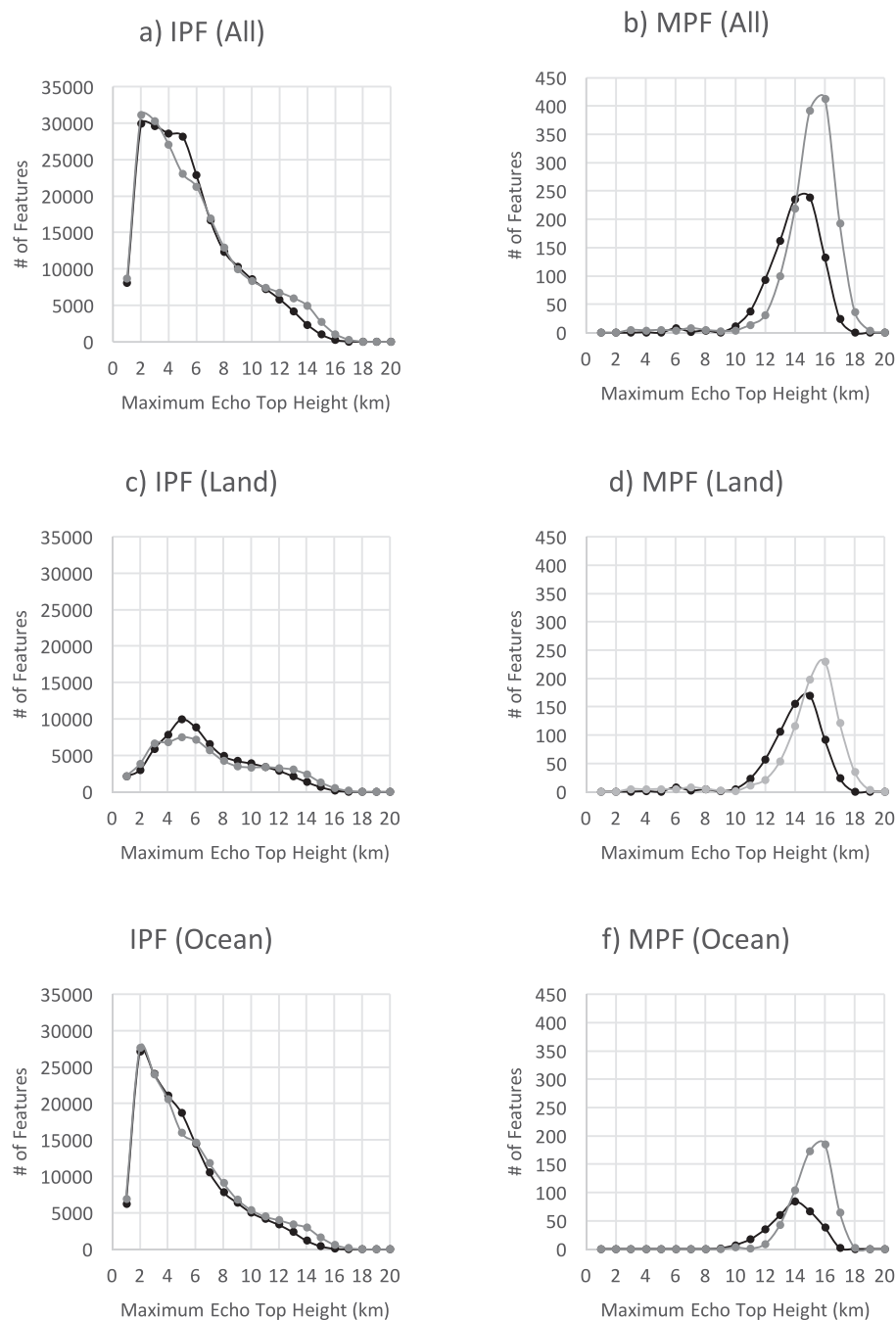
Fig. 12. Maximum IPF and MPF height distribution during 0000 UTC 17 June to 0000 UTC 23 June 2010 for WRF-CC (black) and WRF-RCP8.5 (gray) for land and ocean.

increased dramatically, in line with previous studies that showed an increase in precipitation in a future warmer climate (e.g., O'Gorman, 2015; Min et al., 2011). When compared to the current climate simulation, precipitation increases in the future warmer climate were much larger over the ocean than over land. In terms of organization, the largest precipitation increases were brought about by oceanic IPF and MPF, followed by land MPF in the northern baroclinic region and over Florida. Land-based IPF precipitation did not change notably overall, but weakened slightly in the coastal plain of the SE US where a stronger future climate NASH may have suppressed precipitation. In addition, the result that ocean-based IPF precipitation increased while land-based IPF stayed the same suggests that the surface flux of water vapor (greater over warming ocean than land) was a key regulator of IPF precipitation. Precipitation intensity, as inferred from the frequency

distributions of rainrates and maximum height of precipitation features, increased for both IPF and MPF in the warmer climate. The most notable precipitation intensity increases occurred in oceanic MPFs, with feature height increases of as much as 2 km and with large rainrate increases at the high rainrate end of the spectrum of as much as 40 mm hr/h. Land-based IPF underwent small precipitation intensity changes in the future climate. Overall, the increased feature heights in the warmer climate were consistent with the increases in CAPE and depth of the troposphere. Though this is a short case study, the results presented here suggest that as the climate warms the largest increases in instantaneous extreme precipitation may be associated with mesoscale organization over the ocean. Also since IPF precipitation fractions decreased and MPF sizes increased, the future climate seems to have undergone a general increase in mesoscale organization. Another

significant result of this study is a dramatic change in the diurnal cycle of oceanic IPF. In the future climate precipitation increased throughout the day while maintaining a maximum in the late afternoon and a minimum near midnight. The amplitude of the diurnal cycle of IPF over the ocean, however, nearly doubled with a large morning peak that surpassed the afternoon peak over land.

This study demonstrates that the application of a simple precipitation feature identification algorithm to WRF simulations can give valuable insight into the effect of climate change upon precipitation organization. In particular, the distinction between the effects of climate change on IPFs and MPFs may lead to a better understanding of the mechanisms through which climate change may increase precipitation intensity at the extreme precipitation end of the spectrum, where MPFs seem to be the dominant mode of precipitation. A future study using longer model simulations is needed to provide more robust statistics concerning the effects of climate change on precipitation organization.

Acknowledgements

References

Allen, M.R., Ingram, W.J., 2002. Constraints on future changes in climate and the hydrologic cycle. Nature 419 (6903), 224–232. https://doi.org/10.1038/nature01092.

Barnes, E., Polvani, L., 2013. Response of the midlatitude jets, and of their variability, to increased greenhouse gases in the CMIP5 Models. J. Clim. 26, 7117–7135. https://doi.org/10.1175/JCLI-D-12-00536.1.

Bengtsson, L., Hodges, K.I., Roeckner, E., 2006. Storm Tracks and climate Change. J. Clim. 19, 3518–3543. https://doi.org/10.1175/JCLI3815.1.

Bengtsson, L., Hodges, K.I., Keenlyside, N., 2009. Will extratropical cyclones intensify in a warmer climate? J. Climate 22, 2276–2301. https://doi.org/10.1175/2008JCLI2678.1.

Booth, J.F., Polvani, L., 2013. Midlatitude storms in a moister world: lessons from idealized baroclinic life cycle experiments. Clim. Dyn. 41, 787–802. https://doi.org/10.1007/s00382-012-1472-3.

Carbone, R.E., Tuttle, J.D., 2008. Rainfall occurrence in the US warm season: the diurnal cycle. J. Clim. 21 (6), 4132–4146.

CISL (Computational and Information Systems Laboratory), 2012. Yellowstone: IBM iDataPlex System (Climate Simulation Laboratory). National Center for Atmospheric Research, Boulder, CO. http://n2t.net/ark:/85065/d7wd3xhc.

Flato, G., et al., 2013. Evaluation of climate Models. In: Intergovernmental Panel on climate Change, ed. climate Change 2013 - the Physical Science Basis. Cambridge University Press, Cambridge, pp. 741–866. Available at: http://ebooks.cambridge.org/ref/id/CBO9781107415324A028.

Frei, C., Schär, C., Lüthi, D., Davies, H., 1998. Heavy precipitation processes in a warmer climate. Geophys. Res. Let. 25 (9), 1431–1434. https://doi.org/10.1029/98GL51099.

Hara, M., Kawase, H., Yoshikane, T., Kimura, F., 2008. Estimation of the impact of global warming on snow depth in Japan by the Pseudo-Global-Warming Method. Hydrological Research Letters 2 (5), 61–64. https://doi.org/10.3178/HRL.2.61.

Held, I.M., Soden, B.J., 2006. Robust responses of the hydrological cycle to global warming. J. Clim. 19 (21), 5686–5699. https://doi.org/10.1175/JCLI3990.1.

Hennessy, K., Gregory, J., Mitchell, J., 1997. Change in daily precipitation under enhanced greenhouse conditions. Clim. Dyn. 13, 667–680. https://doi.org/10.1007/s003820050189.

Hill, K.A., Lackmann, G.M., 2011. The impact of future climate change on TC intensity and structure: a downscaling approach. J. Clim. 24 (17), 4644–4661. https://doi.org/10.1175/2011JCLI3761.1.

Hong, S., Lim, J., 2006. The WRF single-moment 6-class microphysics scheme (WSM6). Journal of the Korean Meteorological Society 42 (2), 129–151.

Hong, S.Y., Dudhia, J., Chen, S.H., 2004. A revised Approach to Ice Microphysical Processes for the Bulk Parameterization of Clouds and Precipitation. Mon. Wea. Rev. 132 (1), 103–120. https://doi.org/10.1175/1520-0493(2004)132<0103:ARATIM>2.0.CO;2.

Hong, S.Y., Noh, Y., Dudhia, J., 2006. A New Vertical Diffusion Package with an Explicit Treatment of Entrainment Processes. Mon. Wea. Rev. 134 (9), 2318–2341. https://doi.org/10.1175/MWR3199.1.

Houze, R.A., 1989. Observed structure of mesoscale convective systems and implications for large-scale heating. Q. J. Roy. Met. Soc. 115 (487), 425–461. https://doi.org/10.1002/qj.49711548702.

Iacono, M.J., Delamere, J.S., Mlawer, E.J., Shephard, M.W., Clough, S.A., Collins, W.D., 2008. Radiative forcing by long-lived greenhouse gases: Calculations with the AER radiative transfer models. J. Geophys. Res. 113 (D13). https://doi.org/10.1029/2008JD009944.

IPCC, 2014. Climate Change 2014: Synthesis Report. In: Core writing Team, Pachauri, R.K., Meyer, L.A. (Eds.), Contribution of Working groups I, II and III to the Fifth Assessment Report of the Intergovernmental Panel on climate Change. IPCC, Geneva, Switzerland 151 pp.

Janjić, Z.I., 1994. The Step-Mountain Eta Coordinate Model: further Developments of the Convection, Viscous Sublayer, and Turbulence Closure Schemes. Mon. Wea. Rev. 122 (5), 927–945. https://doi.org/10.1175/1520-0493(1994)122<0927:TSMECM>2.0.CO;2.

Kanada, S., Wada, A., Sugi, M., 2013. Future changes in structures of extremely intense tropical cyclones using a 2-km mesh nonhydrostatic model. J. Clim. 26 (24), 9986–10005. https://doi.org/10.1175/JCLI-D-12-00477.1.

Kawase, H., Yoshikane, T., Hara, M., Kimura, F., Yasunari, T., 2008. Downscaling of the Climatic Change in the Mei-yu Rainband in East Asia by a Pseudo climate simulation Method. SOLA 4 (c), 73–76. https://doi.org/10.2151/sola.2008-019.

Kharin, V.V., Zwiers, F.W., Zhang, X., Hegerl, G.C., 2007. Changes in Temperature and Precipitation Extremes in the IPCC Ensemble of Global Coupled Model Simulations. J. Clim. 20 (8), 1419–1444. https://doi.org/10.1175/JCLI4066.1.

Kimura, F., Kitoh, A., 2007. Downscaling by Pseudo Global Warning Method. The Final Report of ICCAP 10, 2–5. Available at: http://www.chikyu.ac.jp/iccap/ICCAP_Final_Report/2/4-climate_kimura.pdf.

Lackmann, G.M., 2013. The South-Central U.S. Flood of May 2010: Present and Future. J. Clim. 26 (13), 4688–4709. https://doi.org/10.1175/JCLI-D-12-00392.1.

Leary, C.A., Houze Jr., R.A., 1979. The structure and evolution of convection in a tropical cloud cluster. J. Atmos. Sci. 36 (3), 437–457. https://doi.org/10.1175/1520-0469(1979)036<0437:TSAEOC>2.0.CO;2.

Li, W., Li, L., Fu, R., Deng, Y., Wang, H., 2011. Changes to the North Atlantic Subtropical High and its Role in the Intensification of Summer Rainfall Variability in the Southeastern United States. J. Clim. 24 (5), 1499–1506. https://doi.org/10.1175/2010JCLI3829.1.

Li, L., Li, W., Deng, Y., 2013. Summer rainfall variability over the southeastern United States and its intensification in the 21st century as assessed by CMIP5 models. J. Geophys. Res. Atmospheres 118 (2), 340–354. https://doi.org/10.1002/jgrd.50136.

Liu, C., et al., 2017. Continental-scale convection-permitting modeling of the current and future climate of North America. Clim. Dyn. 49, 71. https://doi.org/10.1007/s00382-016-3327-9.

Manda, A., et al., 2014. Impacts of a warming marginal sea on torrential rainfall organized under the Asian summer monsoon. Nature Sci. Rep. https://doi.org/10.1038/srep05741.

Mesinger, F., et al., 2006. North American Regional Reanalysis. Bull. Amer. Met. Soc. 87 (3), 343–360.

Min, S.K., Zhang, X., Zwiers, F.W., Hegerl, G.C., 2011. Human contribution to more-intense precipitation extremes. Nature 470, 378–381. https://doi.org/10.1038/nature09763.

Nesbitt, S.W., Zipser, E.J., Cecil, D.J., 2000. A census of precipitation features in the tropics using TRMM: Radar, ice scattering, and lightning observations. J. Clim. 13 (23), 4087–4106. https://doi.org/10.1175/1520-0442(2000)013<4087:ACOPFI>2.0.CO;2.

Nesbitt, S.W., Zipser, E.J., 2003. The Diurnal Cycle of cainfall and convective intensity according to three years of TRMM measurements. J. Clim. 16, 1456–1475. https://doi.org/10.1175/1520-0442(2003)016<1456:TDCORA>2.0.CO;2.

Nesbitt, S., Cifelli, R., Rutledge, S.A., 2006. Storm morphology and rainfall characteristics of TRMM precipitation features. Mon. Wea. Rev. 134, 2702–2721. https://doi.org/10.1175/MWR3200.1.

Nieto Ferreira, R., and Rickenbach, T.M., 2018: Effects of the North Atlantic Subtropical High on summertime precipitation organization in the southeast United States. Submitted to Int. J. Climatol.

O'Gorman, P.A., 2015. Precipitation extremes under climate change. Curr. Clim. Change Rep. 1, 49–59. https://doi.org/10.1007/s40641-015-0009-3.

Pall, P., Allen, M.R., Stone, D., 2007. Testing the Clausius-Clapeyron constraint on changes in extreme precipitation under CO_2 warming. Clim. Dyn. 28 (4), 351–363.

Pendergrass, A.G., Reed, K.A., Medeiros, B., 2016. The link between extreme precipitation and convective organization in a warming climate: global radiative-convective equilibrium simulations. Geophys. Res. Lett. 43, 11445–11452. https://doi.org/10.1002/2016GL071285.

Prat, O.P., Nelson, B.R., 2014. Characteristics of annual, seasonal and diurnal precipitation in the Southeastern United States derived from long-term remotely sensed data. Atmos. Res. 144, 4–20.

Prein, A.F., et al., 2015. A review on regional convection-permitting climate modeling: demonstrations, prospects, and challenges. Rev. Geophys. 53, 323–361. https://doi.org/10.1002/2014RG000475.

Rasmussen, R., et al., 2011. High-resolution coupled climate runoff simulations of seasonal snowfall over Colorado: a process study of current and warmer climate. J. Clim. 24 (12), 3015–3048. https://doi.org/10.1175/2010JCLI3985.1.

Rasmussen, K.L., Prein, A.F., Rasmussen, R.M., Ikeda, K., Liu, C., 2017. Changes in the convective population and thermodynamic environments in convection-permitting regional climate simulations over the United States. Clim. Dyn. https://doi.org/10.

1007/s00382-017-4000-7.

Rickenbach, T.M., Rutledge, S., 1998. Convection in TOGA COARE: Horizontal scale, morphology and rainfall production. J. Atmos. Sci. 55, 2715–2729. https://doi.org/10.1175/1520-0469(1998)055<2715:CITCHS>2.0.CO;2.

Rickenbach, T.M., Nieto-Ferreira, R., Barnhill, R., Nesbitt, S., 2011. Regional contrast of mesoscale convective system structure prior to and during monsoon onset across South America. J. Clim. 24, 3753–3763. https://doi.org/10.1175/2011JCLI3975.1.

Rickenbach, T.M., Nieto-Ferreira, R., Barnhill, R., Nesbitt, S., 2013. Seasonal and regional differences in the rainfall and intensity of isolated convection over South America. Int. J. Climatol. 33, 2002–2007. https://doi.org/10.1002/joc.3568.

Rickenbach, T.M., Nieto-Ferreira, R., Zarzar, C., Nelson, B., 2015. A seasonal and diurnal climatology of precipitation organization in the southeastern United States. Q. J. Roy. Met. Soc. 141, 1938–1956. https://doi.org/10.1002/qj2500.

Sanford, T., Frumhoff, P.C., Luers, A., Gulledge, J., 2014. The climate Policy Narrative for a Dangerously Warming World. Nat. Clim. Chang. 4 (3), 164–166. https://doi.org/10.1038/nclimate2148.

Sato, T., Kimura, F., Kitoh, A., 2007. Projection of global warming onto regional precipitation over Mongolia using a regional climate model. J. Hydrol. 333 (1), 144–154. https://doi.org/10.1016/j.jhydrol.2006.07.023.

Schär, C., Lüthi, D., Davies, H.C., 1996. Surrogate climate-change scenarios for regional climate models. Geophys. Res. Let. 23 (6), 669–672. https://doi.org/10.1029/96GL00265.

Schumacher, C., Houze, R.A., Kraucunas, I., 2004. The Tropical Dynamical Response to Latent heating estimates Derived from the TRMM Precipitation Radar. J. Atmos. Sci. 61 (12), 1341–1358. https://doi.org/10.1175/1520-0469(2004)061<1341:TTDRTL>2.0.CO;2.

Skamarock, W.C., Klemp, J., Dudhia, J., Gill, D.O., Barker, D.M., Duda, M.G., Huang, X.-Y., Powers, J.G., 2008. A Description of the Advanced Research WRF Version 3. In: Technical Report, pp. 113 June.

Taylor, K.E., Stouffer, R.J., Meehl, G.A., 2012. An overview of CMIP5 and the experiment design. Bull. Amer. Met. Soc. 93 (4), 485–498. https://doi.org/10.1175/BAMS-D-11-00094.1.

Tewari, M., Wang, W., Chang, F., Cuenca, R., 2004. Implementation and verification of the unified Noah land surface model in the WRF model. Bull. Amer. Met. Soc. 2165–2170.

Thiébaux, J., Rogers, E., Wang, W., Katz, B., 2003. A new high-resolution blended real-time global sea surface temperature analysis. Bull. Amer. Met. Soc. 84 (5), 645–656.

Trapp, R.J., Hoogewind, K.A., 2016. The realization of extreme tornadic storm events under future anthropogenic climate change. J. Clim. https://doi.org/10.1175/JCLI-D-15-0623.1.

Trenberth, K.E., Dai, A., Rasmussen, R.M., Parsons, D.B., 2003. The changing character of precipitation. Bull. Am. Meteorol. Soc. 84, 1205–1217.

Tsunematsu, N., Kuze, H., Sato, T., Hayasaki, M., Cui, F., Kondoh, A., 2011. Potential impact of spatial patterns of future atmospheric warming on Asian dust emission. Atmos. Environ. 45 (37), 6682–6695. https://doi.org/10.1016/j.atmosenv.2011.08.048.

Wang, H., Fu, R., Kumar, A., Li, W., 2010. Intensification of Summer Rainfall Variability in the Southeastern United States during recent decades. J. Hydrometeorol. 11 (4), 1007–1018. https://doi.org/10.1175/2010JHM1229.1.

Westra, S., Alexander, L.V., Zwiers, F.W., 2013. Global increasing trends in annual maximum daily precipitation. J. Clim. 26, 3904–3918. https://doi.org/10.1175/JCLI-D-12-00502.1.

Willison, J., Robinson, W.A., Lackmann, G.M., 2015. North Atlantic Storm-Track Sensitivity to Warming increases with Model Resolution. J. Clim. 28 (11), 4513–4524. https://doi.org/10.1175/JCLI-D-14-00715.1.

Yoshikane, T., Kawase, H., Kimura, F., Nozawa, T., 2012. Verification of the Performance of the Pseudo-Global-Warming Method for Future climate changes during June in East Asia. SOLA 8, 133–136. https://doi.org/10.2151/sola.2012-033.

Zhang, J., Howard, K., Vasiloff, S., Langston, C., Kaney, B., Arthur, A., Van Cooten, S., Kelleher, K., Kitzmiller, D., Ding, F., 2011. National Mosaic and QPE (NMQ) system: description, results, and future plans. Bull. Amer. Met. Soc. 92, 1321–1338.